

Efficient Thermally Evaporated Perovskite Light-Emitting Devices via a Bilateral Interface Engineering Strategy

Li Song,* Lixin Huang, Yuan Liu, Xiaoyang Guo,* Chong Geng, Shu Xu, Yuanqin Xia, Yuan Zhang, Nannan Luan, and Yongsheng Hu*



Cite This: *J. Phys. Chem. Lett.* 2021, 12, 6165–6173



Read Online

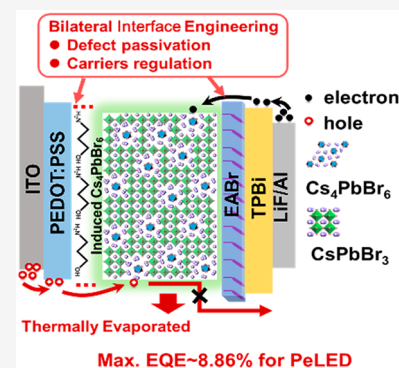
ACCESS |

Metrics & More

Article Recommendations

Supporting Information

ABSTRACT: Physical vapor deposition has emerged as a promising strategy for efficient and stable all-inorganic perovskite light-emitting devices (PeLEDs). However, the thermally evaporated PeLEDs still suffer from unsatisfactory optoelectrical performance because of the massive nonradiative defects. Herein, we demonstrate an efficient bilateral interfacial defect-passivation strategy toward high-performance PeLEDs with a thermally deposited CsPbBr₃ emissive layer (EML). Specifically, the nonradiative defects from the bulk as well as the EML/charge transport layer (CTL) interface are significantly suppressed by implementing the 3-amino-1-propanol (3AP)-modified PEDOT:PSS and introducing ammonium salts, respectively. Simultaneously, both the 3AP induced less-conductive Cs₄PbBr₆ and ammonium salts can balance the charge injection into the EML effectively. As a result, we achieved efficient PeLEDs based on thermally evaporated CsPbBr₃ with a luminance of 15745 cd/m², current efficiency of 32 cd/A, external quantum efficiency of 8.86%, and lifetime of 3.74 h. The strategy proposed here may shed light on the development of highly efficient thermally evaporated PeLEDs.



The past few years have witnessed the astonishing development of metal halide perovskites in optoelectronics, including solar cells, photodetectors, phototransistors and light-emitting devices (LEDs).^{1–4} The superior electroluminescent (EL) performance values, such as high external quantum efficiency (EQE) (>20%),^{5–8} high brightness, flexible color tunability,^{9,10} and narrow emission bandwidth, make the perovskite LEDs (PeLEDs) promising candidates for use in displays.¹¹

Although great progress in solution-processed PeLEDs has been achieved, the unsatisfactory scale-up potential and reproducibility still remain to be solved for future commercialization. Recently, mature thermal vacuum evaporation used in commercial organic LEDs has also attracted increasing attention in manufacturing efficient and reliable all-inorganic perovskite optoelectronics.^{12–18} This intelligent strategy has been successfully adopted to fabricate efficient perovskite solar cells with power conversion efficiency reaching up to ~20%.^{19–21} Although the method also shows great potential in fabricating all-inorganic PeLEDs without considering the low solubility that the raw materials (e.g., CsX or PbX₂, X = Cl, Br, I) suffer, the reported performance of the PeLEDs still lags behind that of the solution-processed counterparts.^{6,10,14–16,22}

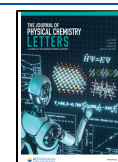
Defect-related low photoluminescence quantum yield (PLQY) and the unbalanced hole and electron transport stemming from either mismatched energy levels or different hole/electron mobilities would be the key factors that limit the EL performance of the PeLEDs. In view of the bulk defects, constructing the core/shell or heterostructure perovskite phase

would be an effective strategy.^{14,23,24} For instance, Lian et al. have demonstrated that Cs₄PbBr₆ can passivate the defects of the CsPbBr₃ to improve the PLQY to ~40% and eventually achieved an EQE of 2.5%.¹⁴ Despite the fact that the optically inactive Cs₄PbBr₆ could passivate the defects, its low conductivity may affect the carrier diffusion in the emissive layer (EML) and thus lead to limited improvement in the EL performance. However, it may conversely be beneficial to confining the carrier spatially in the emissive layer and balancing the hole and electron transport if the distribution of the large-bandgap Cs₄PbBr₆ could be well-controlled. Alternatively, Fu et al. constructed hybrid organic–inorganic 2D–3D perovskite nanostructures to take advantage of the energy-funneling effect to confine the carriers in 3D layers and promote the PLQY to 26.9%, resulting in an unprecedented EQE of 5.3%.²² Apart from the bulk defects, interfacial defects have also played a critical role in the device performance. Replacing the PEDOT:PSS by NiO_x, the luminescence quenching at the hole transport layer/emission layer (HTL/EML) interface was greatly mitigated, advancing the EQE for thermally deposited CsPbBr₃ PeLEDs to 3.26%.¹⁵ Likewise, 2-

Received: May 19, 2021

Accepted: June 21, 2021

Published: June 29, 2021



phenylethanamine bromide (PEABr) was introduced as an ultrathin interlayer between the electron transport layer (ETL)/EML to passivate the nonradiative recombination, resulting in a remarkable improvement in EQE.²⁵ It is well-known that unbalanced hole and electron transport originating from either mismatched energy levels or different hole/electron mobilities would also be an important limitation to the EL performance. Actually, the above-mentioned NiO_x and PEABr can not only suppress the luminescence quenching but also manipulate the carrier transport behaviors, contributing to the high EL performance. These investigations highlight the importance of interfacial defect passivation as well as the carrier balance manipulation.

Herein, we propose a bilateral interfacial engineering to passivate the nonradiative defects and regulate carrier transport to promote the EL performance of the thermally evaporated PeLEDs. The 3AP-doped PEDOT:PSS hole transport layer can facilitate the perovskite phase transformation from CsPbBr₃ to Cs₄PbBr₆ by consuming the unreacted CsBr. The increased amount of Cs₄PbBr₆ can suppress the interfacial defects and block the hole transport simultaneously, resulting in an enhanced PL, better balance between hole and electron carriers, and eventually an improved EL performance. Four kinds of ammonium halides, including PEABr, EABr (ethylammonium bromide), PABr (propylamine hydrobromide) and BABr (butylammonium bromide), were implemented at the ETL/EML interface to further ameliorate the rough morphology caused by 3AP, passivate the residual interfacial defects, and regulate the carrier transport behavior. Consequently, under the synergistic role of 3AP and EABr, the champion device exhibited a brightness of 15745 cd/m², a maximum current efficiency (CE) of 32 cd/A, and a highest EQE of 8.86%. More importantly, our device showed a lifetime of 3.74 h under an initial brightness of 100 cd/m², which is the longest lifetime among the PeLEDs processed by physical-vapor deposition.

Aiming at minimizing the nonradiative defects caused by PEDOT:PSS, we implemented the 3AP to modify PEDOT:PSS as the buried charge transport layer considering that the functional groups of 3AP including -OH and -NH₂ may interact with CsPbBr₃ and affect its crystallization. The 3AP was first dissolved in ethanol at a desired weight ratio and then mixed with PEDOT:PSS at the volume ratio of 1:10 (see more details in [Experimental Methods](#)). For the sake of simplicity and distinction, we denote the samples using the concentrations of 3AP. The perovskite films were fabricated by alternatively depositing CsBr and PbBr₂ (4 pairs in total). The optimal number of pairs was determined according to the device performance ([Figure S1](#)). It is well-known that the crystallinity and morphology of the perovskite are sensitive to the properties of the underlying charge transport layer. Thus, we measured the morphology of the perovskite films deposited on different 3AP-modified PEDOT:PSS. As shown in [Figure 1a–d](#), the crystal sizes of the perovskite films gradually become larger in comparison with that deposited on the pure PEDOT:PSS HTL (control sample) as the 3AP concentration increases, indicating the 3AP's regulation effect on perovskite crystallization. Meanwhile, we also observed a color-variation phenomenon between the samples without 3AP (yellow) and with 3AP (pale yellow) as shown in [Figure S2](#), manifesting a phase transformation or recrystallization under the control of 3AP. As is known, the CsPbBr₃ single crystal presents a dark yellow color;^{26,27} the faded color means the amount of

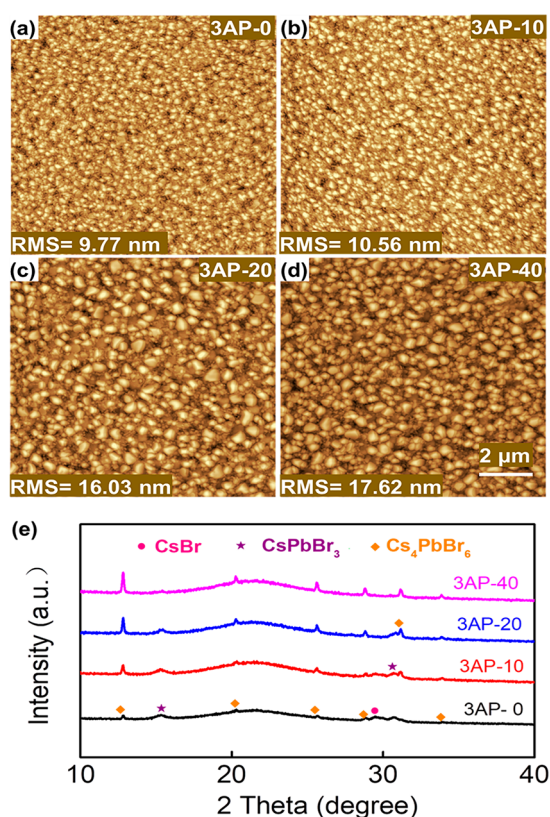
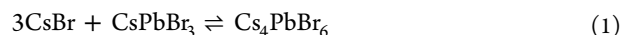


Figure 1. Atomic force microscopy (AFM) images for the thermally evaporated CsPbBr₃ films on PEDOT:PSS with different 3AP concentrations: (a) 3AP-0, (b) 3AP-10, (c) 3AP-20, and (d) 3AP-40. The number in each term stands for the 3AP's concentration in ethanol. (e) X-ray diffraction patterns corresponding to panels a–d.

CsPbBr₃ decreased. X-ray diffraction patterns were performed to investigate the crystallinity evolution as the 3AP concentration increased. As shown in [Figure 1e](#), CsPbBr₃ and Cs₄PbBr₆ coexisted in all the perovskite films. In the control sample, an additional diffraction peak at $2\theta = 29.5^\circ$ corresponding to CsBr also emerged, indicating that the CsBr is excessive and not completely transformed to CsPbBr₃ or Cs₄PbBr₆ in our samples. However, it decreased and completely disappeared when the concentration of 3AP was greater than 20 mg/mL. According to the following transformation relationship between CsPbBr₃ and Cs₄PbBr₆ ([eq 1](#)), the disappeared CsBr indicates the consumption of CsPbBr₃ and increase of Cs₄PbBr₆. The relative diffraction intensity of CsPbBr₃/Cs₄PbBr₆, which decreased as the 3AP concentration increased, confirmed the increased amount of Cs₄PbBr₆ and reduced amount of CsPbBr₃ in the perovskite films. Because the Cs₄PbBr₆ has a large bandgap of ~ 3.9 eV,²⁸ which is transparent in the visible region, the changes in the relative amount of CsPbBr₃/Cs₄PbBr₆ would be expected to alter the film's color, which agrees well with the experimental observations.



The UV–vis absorption spectra of these films in [Figure 2a](#) showed two absorption peaks at 510 and 315 nm, reaffirming the coexistence of CsPbBr₃ and Cs₄PbBr₆. As the 3AP increase, the absorption peak intensity of Cs₄PbBr₆ increased and that of CsPbBr₃ decreased monotonously, suggesting the variation in the relative amount of CsPbBr₃ and Cs₄PbBr₆, which is in line

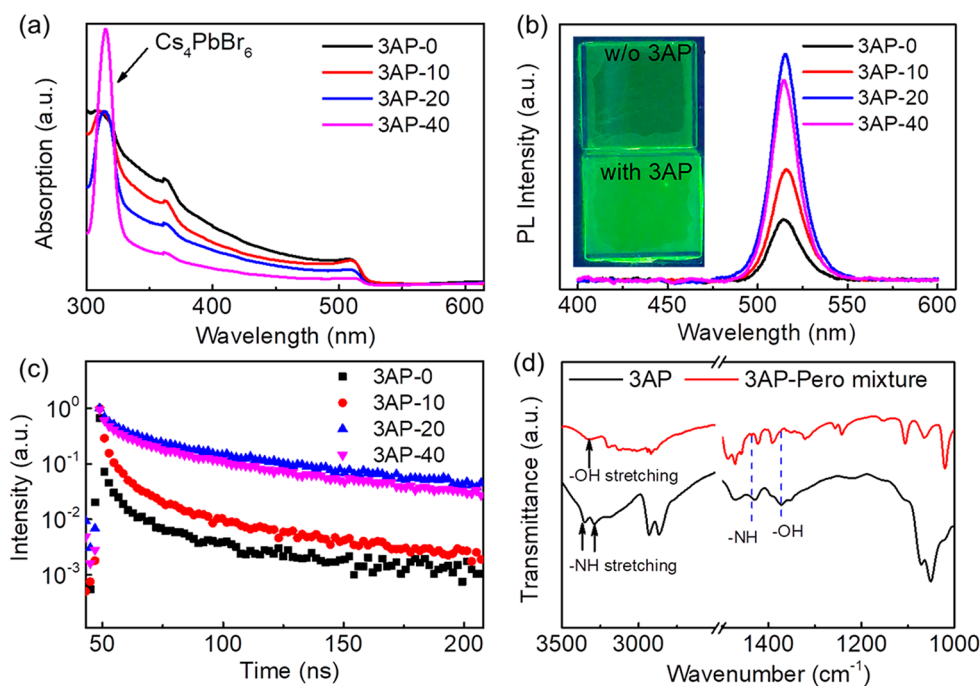


Figure 2. (a) Absorption spectra, (b) PL spectra, and (c) time-resolved photoluminescence for the thermally evaporated Cs–Pb–Br perovskite composites formed on 3AP-PEDOT:PSS with different 3AP doping concentration. (d) FTIR spectra for the 3AP as well as 3AP doped CsBr/PbBr₂ mixture. Inset in panel b is a photograph of the perovskite samples under UV illumination (365 nm).

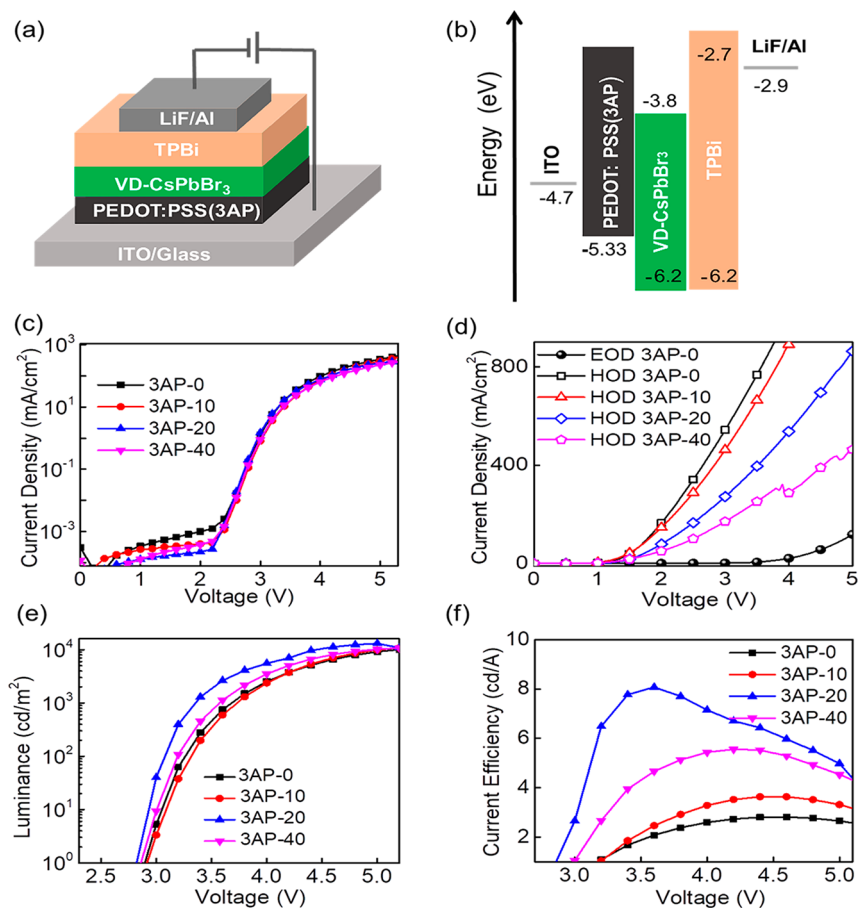


Figure 3. (a) Schematic of LED fabricated using thermally evaporated CsPbBr₃ films. (b) Energy band diagram of the PeLEDs. *J*–*V* curves for the (c) PeLEDs and (d) hole-only devices with different 3AP-modified PEDOT:PSS HTLs. (e) *L*–*V* and (f) CE–*V* characteristics for the PeLEDs with different 3AP-modified PEDOT:PSS HTLs.

with the XRD results. Steady-state PL spectra and time-resolved photoluminescence (TRPL) were measured to evaluate the influence of the 3AP-PEDOT:PSS on the trap states of the perovskite films. As shown in Figure 2b, the PL intensity of perovskite films formed on the 3AP-modified PEDOT:PSS exhibited significant enhancement, in contrast to the control sample, reaching the strongest at 3AP concentration of 20 mg/mL with PLQY of 12.1%. Meanwhile, the average PL lifetime was greatly prolonged from 15.8 ns for the control sample to 90.59 ns for the 3AP-20 sample (also see Table S1). The fastest defects or energy-transfer-related nonradiative recombination component (τ_1) for the 3AP-0 sample was significantly decreased compared with those perovskite films formed on 3AP-PEDOT:PSS. Two factors, including the induced Cs_4PbBr_6 and the changes in the physical properties of PEDOT:PSS, would result in an effective defect passivation and extended excitation lifetime. To verify whether each factor solely plays a role on the exciton recombination kinetics, we constructed a perovskite film without Cs_4PbBr_6 by varying the thickness between CsBr and PbBr_2 . When the thicknesses for CsBr and PbBr_2 were 5 and 3 nm, the absorption peak corresponding to the Cs_4PbBr_6 disappeared, as shown in Figure S3a. Meanwhile, the average exciton lifetime for the 3AP sample is 3.44 ns (Figure S3b), which is slightly longer than that for the sample without 3AP (2.62 ns), indicating that the changes in the PEDOT:PSS also contributed to the PL decay. In addition, we note the lifetime with the low CsBr/ PbBr_2 ratio (5 nm/3 nm) is much decreased in comparison to that with CsBr/ PbBr_2 (11 nm/3 nm) in which Cs_4PbBr_6 existed obviously. Such observations reconfirmed the passivation role of Cs_4PbBr_6 . In summary, the increased exciton lifetime could be due to a collaborative role of 3AP-induced Cs_4PbBr_6 and 3AP-modified PEDOT:PSS. We further performed Fourier-transform infrared (FTIR) spectroscopy to confirm the interaction between 3AP and Cs–Pb–Br-based solid-state powders. Compared with the pure 3AP, the characteristic –NH stretching vibration (asymmetric stretching at 3353 cm^{-1} and symmetric stretching at 3290 cm^{-1}) was greatly weakened in the 3AP–perovskite mixture. More importantly, a new peak at 1436 cm^{-1} which could be ascribed to the symmetric N–H umbrella band appeared in the 3AP–perovskite mixture, implying the existence of the protonated $-\text{NH}_3^+$ terminal group of the 3AP molecule.²⁹ These above results clearly demonstrated that 3AP bonds with the perovskite. Besides this change, the absorption peak at 1372 cm^{-1} which was attributed to the –OH group disappeared compared to the pure 3AP sample, indicating a removal of protons from the hydroxyl group.³⁰ Such interaction may occur between the 3AP and bromide in the perovskite through the hydrogen bond of $-\text{OH}\cdots\text{Br}^-$, which was analogous to the well-known interaction between electrophilic functional groups and I^- .^{31–33} Overall, the above results manifested that 3AP-PEDOT:PSS could stimulate the formation and recrystallization of Cs_4PbBr_6 , resulting in defect suppression and PL enhancement.

Inspired by the defect suppression and enhanced radiative recombination of the EML on the 3AP-modified PEDOT:PSS, we further built multilayered light-emitting devices with structure of ITO/3AP-PEDOT:PSS/EML/TPBi/LiF/Al (Figure 3a) to investigate its impact on the EL performance. The corresponding energy level alignment is displayed in Figure 3b. The 3AP-modified PEDOT:PSS exhibited a deeper work function (see Figure S4) of 5.33 eV compared with the pure

PEDOT:PSS ($\sim 4.9\text{--}5.0\text{ eV}$).^{3,34} This variation would mitigate the energy barrier and thus promote the hole injection into the EML. Figure 3c,e,f present the electroluminescent characteristics, and key parameters are summarized in Table 1. Despite

Table 1. Summary of the Optoelectrical Performance for the PeLEDs with Different Interfacial Modifications

3AP concn. (mg/mL)	ammonium halides	PLQY (%)	V_{on} (V)	L_{max} (cd m^{-2})	CE_{max} (cd A^{-1})	EQE_{max} (%)
w/o	w/o	4.9	2.9	10876	2.81	0.78
10	w/o	5.4	2.9	11119	3.63	1.01
20	w/o	12.1	2.9	14725	8.07	2.24
20	PEABr	27.5	2.9	21581	22.78	6.31
20	EABr	29.4	2.8	15745	32.00	8.86
20	PABr	13.8	2.9	14285	18.12	5.02
20	BABr	15.3	2.9	23267	17.80	4.93
40	w/o	10.1	2.9	10894	5.55	1.54

the evidently roughened morphology (RMS of 9.77 nm for the control sample and 16.03 nm for the brightest 3AP-20 sample), all the devices exhibited similar relatively low leakage current when working under the turn-on voltage ($<3.0\text{ V}$). We also observed that the current density circulating in the device at high voltage reduced after the introduction of 3AP in PEDOT:PSS (also see Figure S5). Considering the increment of less-conductive Cs_4PbBr_6 , the hole transport ability may be reduced. To confirm our conjecture, hole-only devices with a structure of ITO/PEDOT:PSS or 3AP-PEDOT:PSS/perovskite/HAT-CN/Al (see Figure S6) were constructed. Meanwhile, electron-only devices with structure of ITO/LiF/perovskite/TPBi/LiF/Al were also fabricated to investigate the electron transport properties in our devices. As shown in Figure 3d, the hole current density was much higher than the electron current density, suggesting a serious imbalance between holes and electrons which is detrimental to the device performance. The unbalanced charge transport would be responsible for the poor EL performance of the control device with CE of only 2.81 cd/A . After the introduction of 3AP, the hole current decreased monotonically as the 3AP concentration increased, agreeing well with the current behaviors of the PeLEDs with different 3AP-PEDOT:PSS and resulting in a better charge-carrier balance. In addition, quantitative analysis on the hole-only device (Figure S7) also revealed that the trap density has been significantly reduced from $4.76 \times 10^{17}\text{ cm}^{-3}$ for the 3AP-0 sample to $3.19 \times 10^{17}\text{ cm}^{-3}$ for the 3AP-20 sample. As a result, the EL performance was dramatically promoted. The maximum brightness was improved from 10876 cd/m^2 (3AP-0) to 14725 cd/m^2 (3AP-20), and the CE value was evidently improved to 8.07 cd/A (Figure 3e,f).

Although the charge-carrier balance and the radiative recombination have been ameliorated by the 3AP-PEDOT:PSS stimulated Cs_4PbBr_6 to some extent, the hole carriers flowing through the PeLEDs still surpass the electron carriers (see Figure 3d), which would limit the further improvement of the EL performance. Moreover, there would also exist nonradiative traps at the rough EML grain boundaries as well as the EML/ETL interface. Therefore, it is necessary to introduce a suitable interlayer to further balance hole and electron transport, reduce the surface roughness, and advance the radiative recombination. According to our previous work, it is found that the insulating ammonium

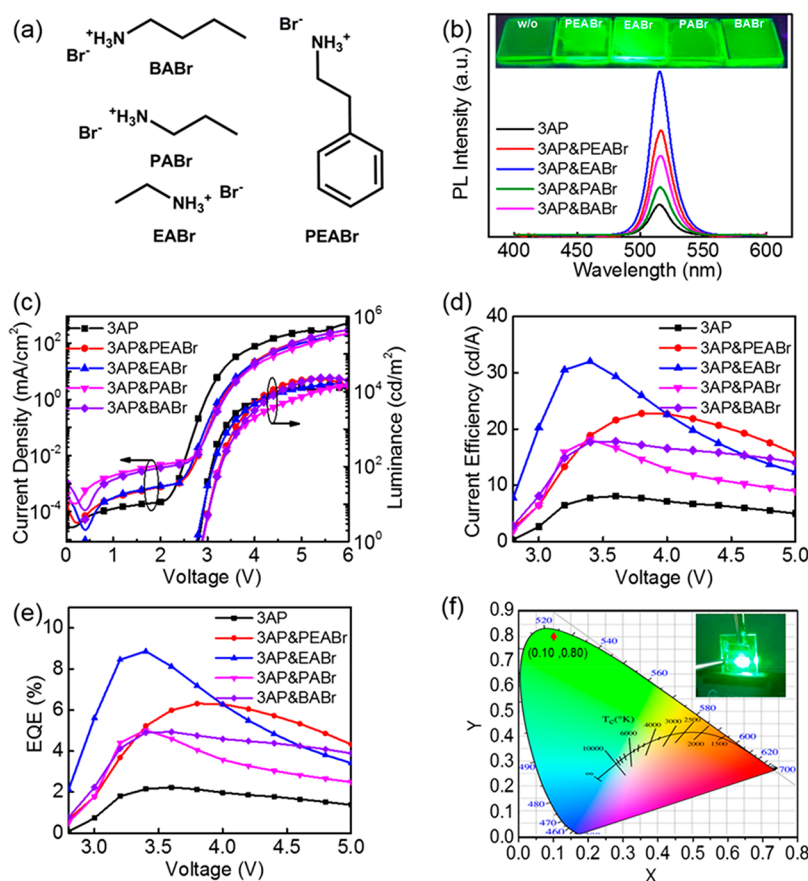


Figure 4. (a) Molecular structure of the ammonium halides. (b) PL spectra for the perovskite films after the modification of ammonium halides. Insets are the corresponding photographs under UV illumination. (c) J - V - L curves, (d) CE- V curves, and (e) EQE- V curves for the PeLEDs with different interfacial modification layers. (f) CIE coordinates for the PeLEDs. Inset shows the lightened PeLED.

halides can terminate on the CsPbBr₃ surface to suppress the nonradiative recombination and regulate the charge transport simultaneously.²⁵ Borrowing from this strategy, we introduced another interfacial layer to further advance the EL performance. Four kinds of ammonium halides with different side-chain structures (illustrated in Figure 4a), named PEABr, EABr, PABr, and BABr, were implemented in our work. Taking into account the difference in defect passivation and insulation properties between these ammonium halides, their individual optimal thickness would also be different. We first cautiously investigated the effect of different thicknesses of ammonium salts on device performance to determine the optimal thickness. Actually, the definite thickness of these ultrathin interfaces was difficult to determinate accurately owing to the rough topographies (shown in Figure S8). Therefore, we distinguish their thickness using the weight concentration. The performance for the PeLEDs with the sole ETL/EML interfacial modification (Figure S9 and Table S2) was also greatly improved in comparison to that without any modification, agreeing well with our previous investigation.²⁵ The maximum current efficiencies reached 16.94, 19.21, 15.01, and 15.15 cd/A for the PEABr (0.5 mg/mL), EABr (0.75 mg/mL), PABr (0.5 mg/mL), and BABr (0.5 mg/mL) modified PeLEDs, respectively. Upon finding the optimal concentration of 3AP and the ammonium salts, it is expected that their combination in the bilateral interfacial engineering would contribute to more excellent EL performance. Encouragingly, the nonradiative defects were further passivated as evidenced

by the brighter PL emission after introducing the ammonium salts (see Figure 4b) in stark contrast to the sample with merely 3AP modification. Moreover, the PL profiles were not affected by the ammonium halides, as evidenced by the normalized PL spectra in Figure S10a. Notably, the sample with the EABr interface showed the strongest light emission (PLQY \approx 29.4%). The possible reason may be that EA⁺ has the smallest ion radius and can easily penetrate into the deeper grain-boundaries to passivate the trap states, as evidenced by the reduced surface roughness shown in Figure S8. Previous investigation demonstrated that the EA⁺ can fill into the crystal lattice to form alloyed EA_xCs_{1-x}PbBr₃ ($0 < x < 1$).³⁵ The incorporation of a larger cation into the CsPbBr₃ lattice will alter the electronic coupling between Pb and Br atoms in PbBr₆⁴⁻ octahedra, resulting in a larger bandgap for EA_xCs_{1-x}PbBr₃. Although there is no corresponding blue-shifted PL spectra for the EA_xCs_{1-x}PbBr₃, it is still tricky to determine whether this alloyed perovskite phase is formed because energy-funneling from EA_xCs_{1-x}PbBr₃ to CsPbBr₃ would occur from EA_xCs_{1-x}PbBr₃ with larger bandgap to CsPbBr₃ with narrower bandgap. We also performed transient absorption (TA) measurement to investigate whether there existed a multiphase or not. As shown in Figure S11, for the perovskite film both with and without EABr passivation, only one ground-state photobleaching signal corresponding to the bulk CsPbBr₃ phase for both perovskite films can be clearly observed for the EABr-incorporated perovskite film, excluding the formation of a distinctive perovskite with larger bandgap.

In total, it is clear that the defects were greatly suppressed after the introduction of the EABr interlayer.

From the lower current densities for the ammonium bromide modified PeLEDs after turn-on voltage (Figure 4c), we can safely conclude that carrier transport is further regulated by the insulating ammonium bromide salts. In our previous investigation, it was found that insulating PEABr can block both hole and electron transport and the blocking effect on the former is greater than on the latter.²⁵ Therefore, the decreased current density originating from a stronger hole-blocking effect and weaker electron-blocking effect could contribute to a better carrier balance for the PeLEDs. We note the hole-only device with structure of ITO/3AP-PEDOT:PSS/perovskite/EABr (0.75 mg/mL)/HAT-CN/Al exhibited J - V characteristics similar to those of the electron-only device (Figure S12), demonstrating a balanced charge carrier transport. Profiting from the further surface passivation and carrier regulation, the CE values are promoted to 22.78, 32, 18.12, and 17.8 cd/A and corresponding EQE values are improved to 6.31, 8.86, 5.02, and 4.93% for PEABr, EABr, PABr, and BABr modified PeLEDs, respectively (Figure 4d,e). To the best of our knowledge, the EQE of 8.86% could be the best for the thermally evaporated PeLEDs, demonstrating the feasibility of our bilateral interface engineering. The device with optimal EL performance also showed high reproducibility among 5 separate devices, as shown in Table S3. The voltage-stable EL spectra for the PeLEDs are located at ~ 519 nm with fwhm of 17 nm (Figure S10b) and a pure green CIE 1931 color coordinate of (0.10, 0.80) (Figure 4f), indicating high potential application in display panels.

The influence of this bilateral interface engineering on the working stability of PeLEDs was also investigated. As shown in Figure 5, the PeLED without any interlayer modification can

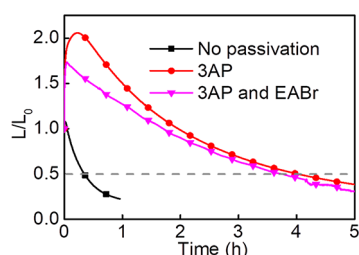


Figure 5. Operational stability for the PeLEDs with or without interface passivation layer.

survive ~ 0.3 h under continuous constant current density drive. In stark contrast, the 3AP-modified PeLED exhibited a much longer time (up to ~ 4 h). The enhancement in operational stability can be ascribed to the efficient defect passivation by the 3AP-induced additional Cs_4PbBr_6 phase. Similar observations have been reported in previous investigation, in which the working stability is greatly improved by $\text{Cs}_4\text{PbBr}_6/\text{CsPbBr}_3$ PeLEDs.^{14,36} However, the trend of operational stability does not follow the trend of EQE. The further introduction of the EABr interface has a detrimental impact on the device stability, resulting in a reduced lifetime of 3.74 h. A recent analysis on the working stability of PEACsPbBr₃ PeLEDs revealed that the reduction in the radiative efficiency and significant changes in J - V characteristics originating from the increased ionic mobility may be the possible reason.³⁷ Much more ongoing work is essential to understand the underlying origin. Although the lifetime is

slightly shortened, it is still much longer than that of the pristine nonmodified PeLEDs, highlighting the importance of this bilateral interfacial defect passivation. Replacing the ionic ammonium halides with the nonionic interface would be one promising methodology to further advance the work stability.

In summary, high-performance PeLEDs with a thermally evaporated CsPbBr_3 emission layer have been realized via suppressing the nonradiative recombination through bilateral interface engineering. The 3AP-modified PEDOT:PSS can stimulate the transformation of optically inactive Cs_4PbBr_6 from CsPbBr_3 by consuming the excess CsBr, leading to the reconstruction of the perovskite component. The increase of Cs_4PbBr_6 can not only passivate the defects but also manipulate the carrier transport, leading to the improvement of the EL performance. The introduction of ammonium halides at the ETL/EML interface can terminate on the CsPbBr_3 surface to passivate the residual defects and further balance the hole and electron transport. Consequently, the PeLED with EABr modification reached the optimal optoelectrical performance with brightness as high as 15745 cd/m^2 , maximum CE of 32 cd/A , and EQE of 8.86%. More importantly, the PeLEDs can exhibit longer lifetime by virtue of the bilateral interfacial defect suppression.

EXPERIMENTAL METHODS

Materials. PbBr_2 (99%), TPBi, PEABr ($\geq 99.5\%$), EABr, PABr, BABr, and PEDOT:PSS (Clevios P AI 4083) were purchased from Xi'an Polymer Light Technology Corp. 4,5,8,9,11-Hexaazatriphenylene-hexacarbonitrile (HAT-CN, 99%) and CsBr (99.999%) were purchased from Aldrich. Isopropanol (IPA) was purchased from Infinity Scientific. LiF (99.99%) was purchased from Innochem. 3AP was purchased from Aladdin. All the chemicals were not further purified and used directly.

Film and Device Fabrication. For the different 3AP doped PEDOT:PSS samples, we first dissolved 3AP in ethanol with desired weight concentration (10, 20, and 40 mg/mL) and then mixed the prepared 3AP-ethanol with the commercial PEDOT:PSS at a volume ratio of 1:10. Prior to the film or device fabrication, the quartz or ITO-coated glass was first ultrasonically cleaned by isopropanol, ethanol, and deionized water in sequence and dried with nitrogen. The substrates were then UV-ozone treated for 20 min and spin-coated with the 3AP-modified PEDOT:PSS at 2500 rpm for 45 s to form the hole transport layer. The PEDOT:PSS was annealed at 140 °C for 10 min in air. The substrates were loaded into a high-vacuum chamber (QHV-R20) to deposit the perovskite layer. The CsBr and PbBr_2 were deposited by thermal evaporation layer-by-layer on the substrate at a rate less than 0.9 and 0.4 Å/s, respectively. Four pairs of CsBr and PbBr_2 were thermally evaporated in total with a CsBr thickness of 11 nm and a PbBr_2 thickness of 3 nm. During the evaporation, the substrate temperature was accurately controlled at 80 °C to facilitate the perovskite crystallization. After the deposition of perovskite film, the samples were transformed to the glovebox and annealed at 100 °C for 30 min for a better solid-phase reaction. For the device fabrication, the as-prepared perovskite films were treated with the ammonium halides (PEABr, EABr, PABr, and BABr), which was dissolved in IPA with a desired weight ratio by spin-coating (4500 rpm for 60s), followed by an annealing process at 70 °C for 10 min. Subsequently, the samples were transformed into the vacuum chamber again, and the electron transport layer TPBi (40 nm), electron injection

layer LiF (1 nm), and cathode Al (100 nm) were deposited successively.

Film and Device Characterization. The UV–vis absorption spectra were obtained using a Persee T6 UV–vis spectrometer. The steady-state PL measurements of perovskite films were performed on a Hitachi fluorescence spectrometer F-7000. The morphologies of perovskite films were obtained on a Shimadzu SPA-9700 atomic force microscope. The time-resolved PL spectra were characterized by an Edinburgh FLS920 spectrometer using a 375 nm laser as an excitation source. The PLQY was measured by FLS920 with an integrating sphere. The thickness of the PbBr₂ and the CsBr were calibrated by a Jobin Yvon Horiba UVISEL ellipsometer. The XRD patterns of the perovskite film were performed by a Rigaku SmartLab. For FTIR measurements (Thermo-Nicolet iS50), the powder was obtained by grinding the mixture of CsBr, PbBr₂, and 3AP at a desired Cs/Pb ratio. The *J–V* characteristics and brightness of the devices were measured using a Keithley 2400 source meter and a luminance meter Konica Minolta LS-160. The electroluminescence spectrum was recorded by an Ocean Optics USB2000+ fiber spectrometer. EQE was calculated based on luminance, current, and EL emission spectrum (assuming Lambertian emission). All the devices were encapsulated using a glass cover with UV glue and measured under ambient atmosphere.

■ ASSOCIATED CONTENT

SI Supporting Information

The Supporting Information is available free of charge at <https://pubs.acs.org/doi/10.1021/acs.jpcllett.1c01592>.

Photographs for the perovskite samples; UPS data for the PEDOT:PSS; electrical or optical characteristics for the hole-only and PeLEDs devices; device structure of the hole-only devices; AFM images for the perovskite films with different ammonium bromides; EL/PL spectra and transient absorption spectra; tables for exciton lifetimes of perovskite films and device performance (PDF)

■ AUTHOR INFORMATION

Corresponding Authors

Li Song – Tianjin Key Laboratory of Electronic Materials and Devices, Hebei Key Laboratory of Advanced Laser Technology and Equipment, School of Electronics and Information Engineering, Hebei University of Technology, Tianjin 300401, P.R. China; orcid.org/0000-0002-4781-4023; Email: songli@hebut.edu.cn

Xiaoyang Guo – State Key Laboratory of Luminescence and Applications, Changchun Institute of Optics, Fine Mechanics and Physics, Chinese Academy of Sciences, Changchun 130033, China; orcid.org/0000-0003-0259-137X; Email: guoxy@ciomp.ac.cn

Yongsheng Hu – School of Physics and Microelectronics, Zhengzhou University, Zhengzhou 450001, China; Email: h0y0s@163.com

Authors

Lixin Huang – Tianjin Key Laboratory of Electronic Materials and Devices, Hebei Key Laboratory of Advanced Laser Technology and Equipment, School of Electronics and Information Engineering, Hebei University of Technology, Tianjin 300401, P.R. China

Yuan Liu – Tianjin Key Laboratory of Electronic Materials and Devices, Hebei Key Laboratory of Advanced Laser Technology and Equipment, School of Electronics and Information Engineering, Hebei University of Technology, Tianjin 300401, P.R. China

Chong Geng – Tianjin Key Laboratory of Electronic Materials and Devices, Hebei Key Laboratory of Advanced Laser Technology and Equipment, School of Electronics and Information Engineering, Hebei University of Technology, Tianjin 300401, P.R. China; orcid.org/0000-0002-7200-6394

Shu Xu – Tianjin Key Laboratory of Electronic Materials and Devices, Hebei Key Laboratory of Advanced Laser Technology and Equipment, School of Electronics and Information Engineering, Hebei University of Technology, Tianjin 300401, P.R. China; orcid.org/0000-0002-4185-1392

Yuanqin Xia – Tianjin Key Laboratory of Electronic Materials and Devices, Hebei Key Laboratory of Advanced Laser Technology and Equipment, School of Electronics and Information Engineering, Hebei University of Technology, Tianjin 300401, P.R. China

Yuan Zhang – Tianjin Key Laboratory of Electronic Materials and Devices, Hebei Key Laboratory of Advanced Laser Technology and Equipment, School of Electronics and Information Engineering, Hebei University of Technology, Tianjin 300401, P.R. China

Nannan Luan – Tianjin Key Laboratory of Electronic Materials and Devices, Hebei Key Laboratory of Advanced Laser Technology and Equipment, School of Electronics and Information Engineering, Hebei University of Technology, Tianjin 300401, P.R. China

Complete contact information is available at: <https://pubs.acs.org/doi/10.1021/acs.jpcllett.1c01592>

Notes

The authors declare no competing financial interest.

■ ACKNOWLEDGMENTS

This work is supported by the Natural Science Foundation of Hebei Province (F2019202252, F2019202294), the Foundation of Hebei Education Department (BJ2021017), the Graduate Innovation Foundation of Hebei Province (CXZZSS2021044), the National Natural Science Foundation of China (Nos. 61774154, 51902082, 61975256, 51973280, 11904323, 62035013, 61675057, and 61975050) and State Key Laboratory of Reliability and Intelligence of Electrical Equipment, Hebei University of Technology (No. EERI-PI2020008).

■ REFERENCES

- (1) Kang, C. H.; Dursun, I.; Liu, G.; Sinatra, L.; Sun, X.; Kong, M.; Pan, J.; Maity, P.; Ooi, E.-N.; Ng, T. K.; et al. High-Speed Colour-Converting Photodetector with All-Inorganic CsPbBr₃ Perovskite Nanocrystals for Ultraviolet Light Communication. *Light: Sci. Appl.* **2019**, *8*, 94.
- (2) Miao, Y.; Cheng, L.; Zou, W.; Gu, L.; Zhang, J.; Guo, Q.; Peng, Q.; Xu, M.; He, Y.; Zhang, S.; et al. Microcavity Top-Emission Perovskite Light-Emitting Diodes. *Light: Sci. Appl.* **2020**, *9*, 89.
- (3) Xie, C.; You, P.; Liu, Z.; Li, L.; Yan, F. Ultrasensitive Broadband Phototransistors Based on Perovskite/Organic-Semiconductor Vertical Heterojunctions. *Light: Sci. Appl.* **2017**, *6*, No. e17023.

- (4) Sun, J.; Wu, J.; Tong, X.; Lin, F.; Wang, Y.; Wang, Z. M. Organic/Inorganic Metal Halide Perovskite Optoelectronic Devices Beyond Solar Cells. *Adv. Sci.* **2018**, *5*, 1700780.
- (5) Cao, Y.; Wang, N.; Tian, H.; Guo, J.; Wei, Y.; Chen, H.; Miao, Y.; Zou, W.; Pan, K.; He, Y.; et al. Perovskite Light-Emitting Diodes Based on Spontaneously Formed Submicrometre-Scale Structures. *Nature* **2018**, *562*, 249–253.
- (6) Lin, K.; Xing, J.; Quan, L. N.; de Arquer, F. P. G.; Gong, X.; Lu, J.; Xie, L.; Zhao, W.; Zhang, D.; Yan, C.; et al. Perovskite Light-Emitting Diodes with External Quantum Efficiency Exceeding 20%. *Nature* **2018**, *562*, 245–248.
- (7) Chiba, T.; Hayashi, Y.; Ebe, H.; Hoshi, K.; Sato, J.; Sato, S.; Pu, Y.-J.; Ohisa, S.; Kido, J. Anion-Exchange Red Perovskite Quantum Dots with Ammonium Iodine Salts for Highly Efficient Light-Emitting Devices. *Nat. Photonics* **2018**, *12*, 681–687.
- (8) Xu, W. D.; Hu, Q.; Bai, S.; Bao, C. X.; Miao, Y. F.; Yuan, Z. C.; Borzda, T.; Barker, A. J.; Tyukalova, E.; Hu, Z. J.; et al. Rational Molecular Passivation for High-Performance Perovskite Light-Emitting Diodes. *Nat. Photonics* **2019**, *13*, 418–424.
- (9) Vashishtha, P.; Ng, M.; Shivarudraiah, S. B.; Halpert, J. E. High Efficiency Blue and Green Light-Emitting Diodes Using Ruddlesden-Popper Inorganic Mixed Halide Perovskites with Butylammonium Interlayers. *Chem. Mater.* **2019**, *31*, 83–89.
- (10) Yusoff, A. R. B. M.; Gavim, A. E. X.; Macedo, A. G.; da Silva, W. J.; Schneider, F. K.; Teridi, M. A. M. High-Efficiency, Solution-Processable, Multilayer Triple Cation Perovskite Light-Emitting Diodes with Copper Sulfide-Gallium-Tin Oxide Hole Transport Layer and Aluminum-Zinc Oxide-Doped Cesium Electron Injection Layer. *Mater. Today Chem.* **2018**, *10*, 104–111.
- (11) Zhang, F.; Song, J.; Han, B.; Fang, T.; Li, J.; Zeng, H. High-Efficiency Pure-Color Inorganic Halide Perovskite Emitters for Ultrahigh-Definition Displays: Progress for Backlighting Displays and Electrically Driven Devices. *Small Methods* **2018**, *2*, 1700382.
- (12) Park, C.-G.; Choi, W.-G.; Na, S.; Moon, T. All-Inorganic Perovskite CsPbI₂Br through Co-Evaporation for Planar Heterojunction Solar Cells. *Electron. Mater.* **2019**, *15*, 56–60.
- (13) Shahiduzzaman, M.; Yonezawa, K.; Yamamoto, K.; Ripolles, T. S.; Karakawa, M.; Kuwabara, T.; Takahashi, K.; Hayase, S.; Taima, T. Improved Reproducibility and Intercalation Control of Efficient Planar Inorganic Perovskite Solar Cells by Simple Alternate Vacuum Deposition of PbI₂ and CsI. *ACS Omega* **2017**, *2*, 4464–4469.
- (14) Lian, X.; Wang, X.; Ling, Y.; Lochner, E.; Tan, L.; Zhou, Y.; Ma, B.; Hanson, K.; Gao, H. Light Emitting Diodes Based on Inorganic Composite Halide Perovskites. *Adv. Funct. Mater.* **2019**, *29*, 1807345.
- (15) Li, J.; Du, P.; Li, S.; Liu, J.; Zhu, M.; Tan, Z.; Hu, M.; Luo, J.; Guo, D.; Ma, L.; et al. High-Throughput Combinatorial Optimizations of Perovskite Light-Emitting Diodes Based on All-Vacuum Deposition. *Adv. Funct. Mater.* **2019**, *29*, 1903607.
- (16) Chen, C.; Han, T.; Tan, S.; Xue, J. J.; Zhao, Y. P.; Liu, Y. F.; Wang, H. R.; Hu, W.; Bao, C.; Mazzeo, M.; et al. Efficient Flexible Inorganic Perovskite Light-Emitting Diodes Fabricated with CsPbBr₃ Emitters Prepared Via Low-Temperature in Situ Dynamic Thermal Crystallization. *Nano Lett.* **2020**, *20*, 4673–4680.
- (17) Du, P.; Li, J.; Wang, L.; Liu, J.; Li, S.; Liu, N.; Li, Y.; Zhang, M.; Gao, L.; Ma, Y.; et al. Vacuum-Deposited Blue Inorganic Perovskite Light-Emitting Diodes. *ACS Appl. Mater. Interfaces* **2019**, *11*, 47083–47090.
- (18) Hu, Y.; Wang, Q.; Shi, Y.-L.; Li, M.; Zhang, L.; Wang, Z.-K.; Liao, L.-S. Vacuum-Evaporated All-Inorganic Cesium Lead Bromine Perovskites for High-Performance Light-Emitting Diodes. *J. Mater. Chem. C* **2017**, *5*, 8144–8149.
- (19) Jang, J.; Choe, G.; Yim, S. Effective Control of Chlorine Contents in MAPbI_{3-x}Cl_x Perovskite Solar Cells Using a Single-Source Vapor Deposition and Anion-Exchange Technique. *ACS Appl. Mater. Interfaces* **2019**, *11*, 20073–20081.
- (20) Longo, G.; Momblona, C.; La-Placa, M.-G.; Gil-Escrig, L.; Sessolo, M.; Bolink, H. J. Fully Vacuum-Processed Wide Band Gap Mixed-Halide Perovskite Solar Cells. *ACS Energy Lett.* **2018**, *3*, 214–219.
- (21) Gil-Escrig, L.; Momblona, C.; La-Placa, M. G.; Boix, P. P.; Sessolo, M.; Bolink, H. J. Vacuum Deposited Triple-Cation Mixed-Halide Perovskite Solar Cells. *Adv. Energy Mater.* **2018**, *8*, 1703506.
- (22) Fu, Y.; Zhang, Q. P.; Zhang, D. Q.; Tang, Y. Q.; Shu, L.; Zhu, Y. Y.; Fan, Z. Y. Scalable All-Evaporation Fabrication of Efficient Light-Emitting Diodes with Hybrid 2D-3D Perovskite Nanostructures. *Adv. Funct. Mater.* **2020**, *30*, 2002913.
- (23) Liu, K.-K.; Liu, Q.; Yang, D.-W.; Liang, Y.-C.; Sui, L.-Z.; Wei, J.-Y.; Xue, G.-W.; Zhao, W.-B.; Wu, X.-Y.; Dong, L.; et al. Water-Induced MAPbBr₃@Pb(OH)₂ with Enhanced Luminescence and Stability. *Light: Sci. Appl.* **2020**, *9*, 44.
- (24) Ma, Z. Z.; Shi, Z. F.; Wang, L. T.; Zhang, F.; Wu, D.; Yang, D. W.; Chen, X.; Zhang, Y.; Shan, C. X.; Li, X. J. Water-Induced Fluorescence Enhancement of Lead-Free Cesium Bismuth Halide Quantum Dots by 130% for Stable White Light-Emitting Devices. *Nanoscale* **2020**, *12*, 3637–3645.
- (25) Jia, K.; Song, L.; Hu, Y.; Guo, X.; Liu, X.; Geng, C.; Xu, S.; Fan, R.; Huang, L.; Luan, N.; et al. Improved Performance for Thermally Evaporated Perovskite Light-Emitting Devices Via Defect Passivation and Carrier Regulation. *ACS Appl. Mater. Interfaces* **2020**, *12*, 15928–15933.
- (26) Stoumpos, C. C.; Malliakas, C. D.; Peters, J. A.; Liu, Z.; Sebastian, M.; Im, J.; Chasapis, T. C.; Wibowo, A. C.; Chung, D. Y.; Freeman, A. J.; et al. Crystal Growth of the Perovskite Semiconductor CsPbBr₃: A New Material for High-Energy Radiation Detection. *Cryst. Growth Des.* **2013**, *13*, 2722–2727.
- (27) Rakita, Y.; Kedem, N.; Gupta, S.; Sadhanala, A.; Kalchenko, V.; Bohm, M. L.; Kulbak, M.; Friend, R. H.; Cahen, D.; Hodes, G. Low-Temperature Solution-Grown CsPbBr₃ Single Crystals and Their Characterization. *Cryst. Growth Des.* **2016**, *16*, 5717–5725.
- (28) Wang, L.; Liu, H.; Zhang, Y.; Mohammed, O. F. Photoluminescence Origin of Zero-Dimensional Cs₄PbBr₆ Perovskite. *ACS Energy Lett.* **2020**, *5*, 87–99.
- (29) Zhang, Y.; Liu, X.; Li, P.; Duan, Y.; Hu, X.; Li, F.; Song, Y. Dopamine-Crosslinked TiO₂/Perovskite Layer for Efficient and Photostable Perovskite Solar Cells under Full Spectral Continuous Illumination. *Nano Energy* **2019**, *56*, 733–740.
- (30) Lin, Z.; Yan, J.; Cai, Q.; Wen, X.; Dong, H.; Mu, C. A Sandwich-Like Electron Transport Layer to Assist Highly Efficient Planar Perovskite Solar Cells. *Nanoscale* **2019**, *11*, 21917–21926.
- (31) González-Pedro, V.; Veldhuis, S. A.; Begum, R.; Bañuls, M. J.; Bruno, A.; Mathews, N.; Mhaisalkar, S.; Maquieira, A. Recovery of Shallow Charge-Trapping Defects in CsPbX₃ Nanocrystals through Specific Binding and Encapsulation with Amino-Functionalized Silanes. *ACS Energy Lett.* **2018**, *3*, 1409–1414.
- (32) Yuan, F. L.; Zheng, X. P.; Johnston, A.; Wang, Y. K.; Zhou, C.; Dong, Y. T.; Chen, B.; Chen, H. J.; Fan, J. Z.; Sharma, G.; et al. Color-Pure Red Light-Emitting Diodes Based on Two-Dimensional Lead-Free Perovskites. *Sci. Adv.* **2020**, *6*, No. eabb0253.
- (33) Zhang, J.; Hu, Z.; Huang, L.; Yue, G.; Liu, J.; Lu, X.; Hu, Z.; Shang, M.; Han, L.; Zhu, Y. Bifunctional Alkyl Chain Barriers for Efficient Perovskite Solar Cells. *Chem. Commun.* **2015**, *51*, 7047–7050.
- (34) Fan, R.; Song, L.; Hu, Y.; Guo, X.; Liu, X.; Wang, L.; Geng, C.; Xu, S.; Zhang, Y.; Zhang, Z.-H.; et al. Boosting the Efficiency and Stability of Perovskite Light-Emitting Devices by 3-Amino-1-Propanol Tailored PEDOT:PSS Hole Transport Layer. *ACS Appl. Mater. Interfaces* **2020**, *12*, 43331–43338.
- (35) Chu, Z.; Zhao, Y.; Ma, F.; Zhang, C.-X.; Deng, H.; Gao, F.; Ye, Q.; Meng, J.; Yin, Z.; Zhang, X.; et al. Large Cation Ethylammonium Incorporated Perovskite for Efficient and Spectra Stable Blue Light-Emitting Diodes. *Nat. Commun.* **2020**, *11*, 4165.
- (36) Shang, Y. Q.; Li, G.; Liu, W. M.; Ning, Z. J. Quasi-2D Inorganic CsPbBr₃ Perovskite for Efficient and Stable Light-Emitting Diodes. *Adv. Funct. Mater.* **2018**, *28*, 1801193.
- (37) Warby, J. H.; Wenger, B.; Ramadan, A. J.; Oliver, R. D. J.; Sansom, H. C.; Marshall, A. R.; Snaith, H. J. Revealing Factors

Influencing the Operational Stability of Perovskite Light-Emitting Diodes. *ACS Nano* **2020**, *14*, 8855–8865.